ISTITUTO NAZIONALE DI FISICA NUCLEARE

Sezione di Milano

On Line Monitoring of the TTF Cryostats Cold Mass with Wire Position Monitors

A. Bosotti, C. Pagani, G. Varisco

INFN–Sezione di Milano–LASA, Via F.lli Cervi 201, I–20090, Segrate (MI), Italy

Abstract

A Wire Position Monitor (WPM) system is used to measure on line the TTF cryomodules alignment stability and reproducibility during cooldown and warm up operations.

This paper reports on the design and realization of the first set of 36 WPMs installed on the first TTF cryomodule, together with the explanation of the electronic read out systems and the analysis of the data acquired during the first three complete thermal cycles of the Linac. A paragraph on the improved WPMs for the other TTF cryomodules can be found at the end of the paper.

PACS.: 07.07.Df

1   INTRODUCTION

The production of affordable cryostats is one of the goals of the TTF project. Each cryostat contains 8 superconducting RF cavities cooled to 2 K, a quadrupole magnet package cooled to 4.5 K, thermal shields at 70 K and 4.5 K, magnetic shielding, cryogenic service pipes and all associated instrumentation. The axes of the 8 cavities must be aligned to the ideal beam axis to within ± 0.5 mm and that of the quadrupole package to within ± 0.1 mm, with an acceptable maximum tilt limited to ± 0.1 mrad. These alignments, performed when the system is warm, must remain fixed after cool down and during operation. Furthermore the cryostat has been designed to prevent that its vibration frequencies could be excited by the RF pulsing at 5 or 10 Hz[1].

A Wire Position Monitor (WPM) system has been developed for on-line monitoring of the cold mass during cooldown and operation. The analysis of the WPM measurements allows checking the alignment reproducibility between successive cooldown cycles. The first cryomodule is equipped with two sets of 18 WPMs, fixed along two straight sections inside the cryostat, to provide a complete 3D analysis of the displacements. A cross section of the first cryomodule showing the two WPM's lines and the titanium supporting arms is shown in fig.1
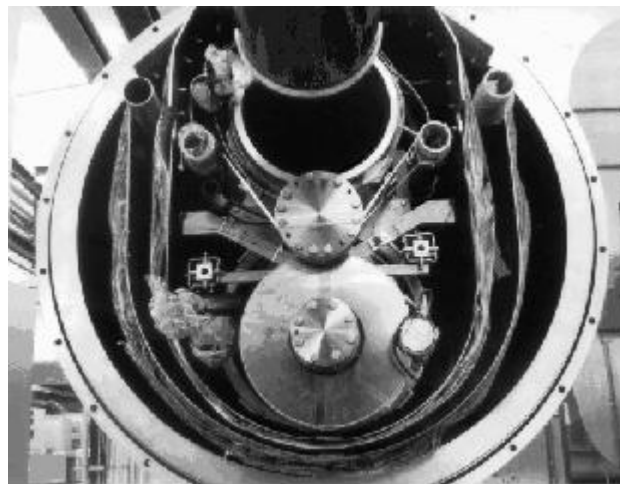
FIG. 1: Cross section of the first TESLA Test Facility (TTF) cryomodule

The schematic layout of two WPMs with their supporting frames is shown in fig. 2. The WPMs are assembled on titanium supporting arms, in order to bind their position to the cold mass active elements (cavities and quadrupole package).

Each WPM has the structure of a beam position monitor, of the microstrip directional coupler type, and it is inserted in a 180 Ω coaxial line fed by a 140 MHz RF signal. The inner conductor is a stretched wire and four symmetric microstrips, attached to the WPM's body, are sampling the applied RF signal.

The body of each WPM is fixed to a cold mass element, while the position of each stretched wire is determined by two external supporting frames. This means that the WPMs move together with the cold mass while the excitation wire is fixed.

Heat treated CuBe (2%) has been chosen for the wire, as a good compromise between RF losses and tensile stress. With a wire diameter of 0.5 mm, we have sag of 2.1 mm with stretching load of 16 kg ($\sim 10^9$ Pa).
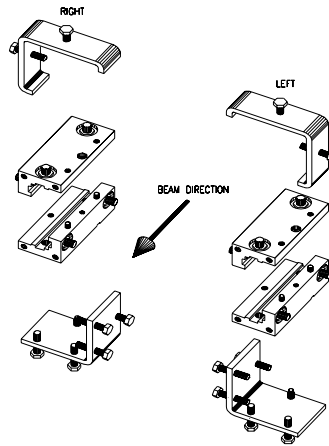
FIG. 2: Two WPMs and their supporting frames.

Both the body of the monitors and the microstrips are made by silver plated bulk aluminum. Aluminum has been chosen to limit the monitor weight, while silver plating is required for RF contact and brazing.
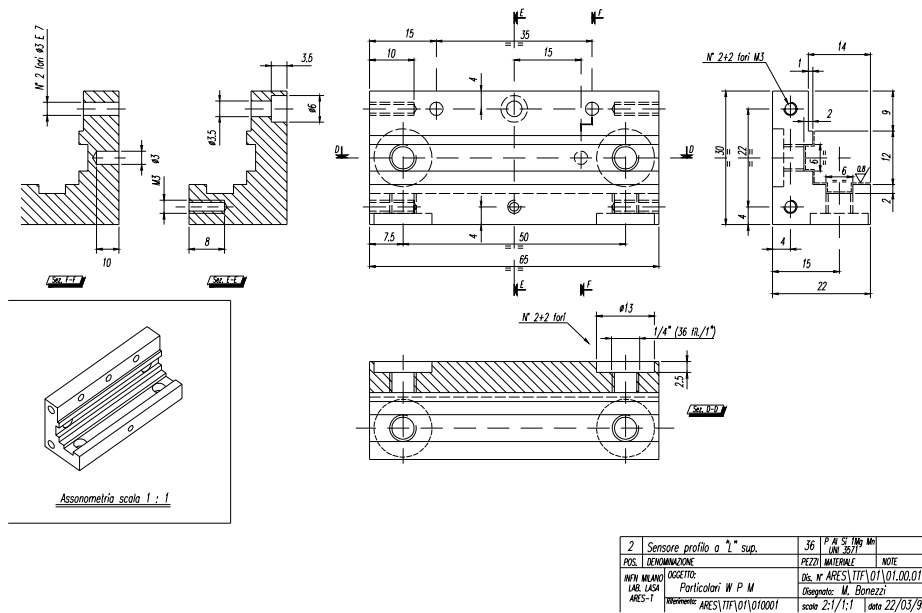
FIG. 3: Details of a WPM.

The microstrips are directly brazed to the SMA connector pins, with no intermediate dielectric material, because of the very wide temperature range, spanning from room temperature to 2 K. LHe tests with different microstrip technologies were done to support this choice. Each monitor is composed of two parts, screwed together after the strips are matched and brazed. The clearance for the wire is 12 mm and the monitor length is 65 mm. Details of a WPM are shown in fig. 3.

A 3D view of one of the two halves of the detector body, without microstrips, is shown in fig. 4 (left), together with the WPM's cross section (right).
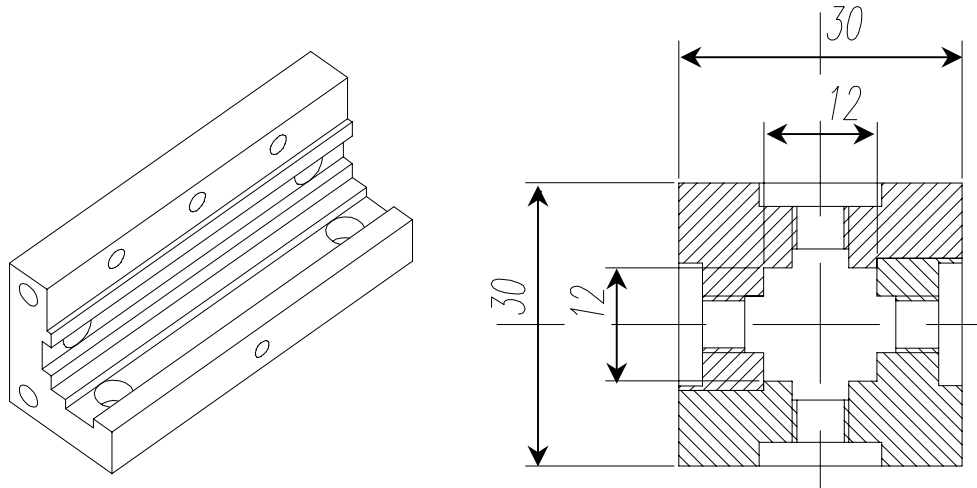
FIG. 4: 3D view (left) and cross section (right) of a WPM.

The external coaxial connecting the monitors is a copper beryllium tube whose internal diameter is 12 mm. Bronze bellows, inserted between the monitors and the coaxial tubes, let the system recover the thermal contraction during the cooldown. Each one of the 9 active elements allocated in a cryomodule is equipped with four WPMs, two for each stretched wire. The two chains of monitors are sketched in Figure 5, where some details are shown concerning the position of the monitors with respect to the relative active element, either for a cavity or the quadrupole package.
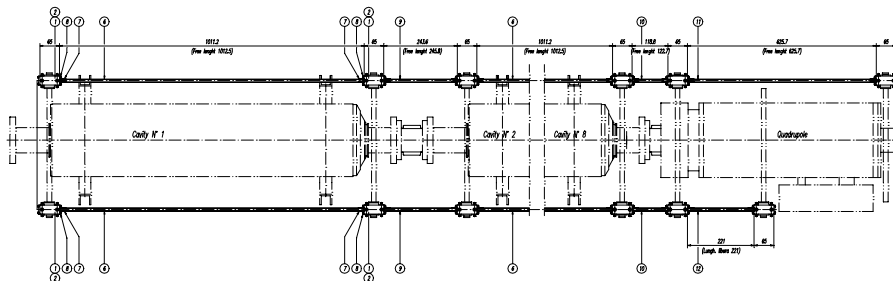
FIG. 5: Top view of the two WPM's chains, showing the position of the monitors with respect to either a cavity or the quadrupole package.
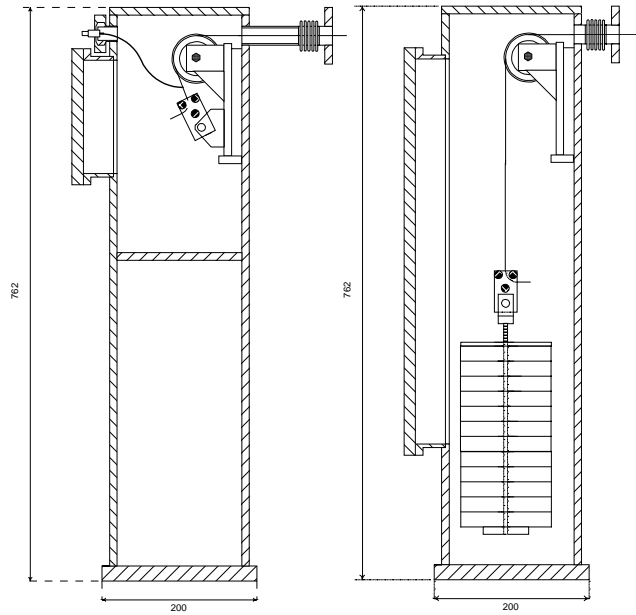
FIG. 6: Boxes for RF input and termination.

The wire connections with the external RF signal and the matching load are made in the two external boxes (for each line) sketched in Fig. 6. Both sides the copper beryllium wires are allowed to slide on insulated brass wheels, while the two wire edges are clamped between epoxy blocks. This is done to accomplish for wire contraction (or expansion) during the cooldown (or warm-up) of the module. One wire edge is fixed, while the other is loaded with a set of lead disks, with a total weight of 16 kg. In this way the tensile strength in the wire stays constant during thermal cycles. The applied tensile strength of $\sim 10^9$ Pa gives sag of about 2 mm at the center of the ~ 13 m long wire.
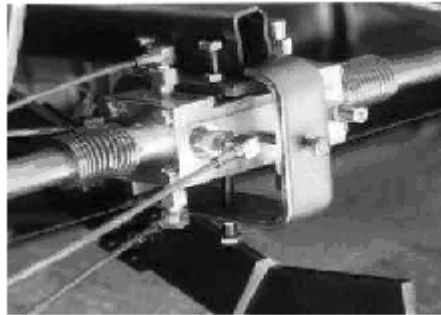
FIG. 7: A WPM installed in the cryostat, showing the supporting frames and its four coaxial cable set.

The WPMs have been installed and aligned in the first cryomodule in spring 1997. In order to guarantee the best linearity in the position measurements, and to make use of all the possible clearance, we plant to position the WPMs following the computed catenary of the stretched wire and 2 mm out of center when warm, to have the wire centered at 2 K. In practice the result has been worst than expected because of the alignment errors in the monitor

positions (± 1 mm) and of the long inaccessible pipes (outer coaxial) at the cryomodule edges. As a consequence the clearance was less than expected and the wire could not be centered at cold. A WPM installed in the cryostat is shown in fig. 7. The screws on the supporting frame are used to adjust the WPM position in the monitors' chain.

1.1 Microstrips

The microstrips, designed for 50 Ω (nominal) impedance, are housed in the WPM's body (see Fig. 8) and soldered to the central pins of two SMA connectors. The upstream port is connected to the readout electronics, while the downstream port is terminated to 50 Ω. The microstrip reference dimensions were set using equation (1)[2]:

$$\frac{w}{h} = \left(\frac{e^H}{8} - \frac{1}{4e^H} \right)^{-1} \tag{1}$$

with

$$H = \frac{Z_0 \sqrt{2(\varepsilon_r + 1)}}{\eta/\pi} + \frac{1}{2}\left(\frac{\varepsilon_r - 1}{\varepsilon_r + 1} \right)\left(\ln\frac{\pi}{2} + \frac{1}{\varepsilon_r}\ln\frac{4}{\pi} \right) \tag{2}$$

where:

w = microstrip width, h = dielectric thickness, Z_0 = characteristic impedance, η = vacuum impedance.
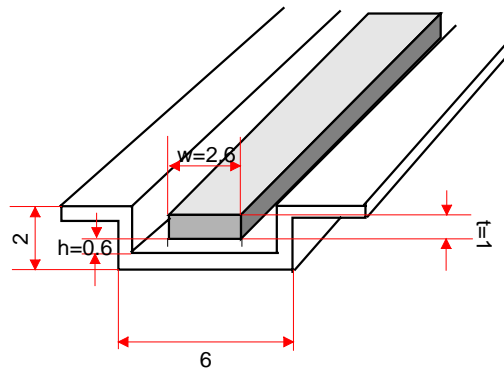
FIG. 8: Microstrip schematics, showing the dimensions.

Choosing w = 2.6 mm, the h nominal value is 0.47 mm. Actually the real dimension were set optimizing "on line" the SWR value, to take into account the microstrip finite thickness (1 mm) and the border effect. With h = 0.6 mm we have the SWR < 1.1 for all the

detectors. One microstrip positioned in the monitor housing is shown in Fig. 8.

Once assembled, with the microstrips and the connectors in place, we have performed tests to check for mechanical stability after abrupt temperature changes. Each device has been immersed ten times in a LN_2 bath (we called it "thermal cycles"). The devices were constantly monitored with a Network Analyzer (set in "Time Reflectometry" mode) when passing from room temperature to LN_2 temperature (and vice versa), to check for possible damages during the cycles. The microstrip "S" parameters have been measured before and after each thermal cycle and a typical set of the values obtained is shown in the Table 1. The positive values of S_{21} and S_{12} at LN_2 are due to the different temperature of the cables, which are included in the calibration of the Network Analyzer at room temperature. No damages were reported in any WPMs after these tests.

TAB. 1: Microstrip S parameters during thermal cycles

Microstrip	Room temperature				LN_2 temperature			
	S_{11}	S_{21}	S_{22}	S_{12}	S_{11}	S_{21}	S_{22}	S_{12}
1	1.0219	-0.012	1.0252	-0.008	1.1327	0.011	1.1308	0.032
2	1.0163	-0.004	1.0146	-0.01	1.0862	0.025	1.0843	0.056
3	1.0021	-0.003	1.0037	-0.0013	1.0933	0.072	1.0935	0.083
4	1.0016	-0.001	1.0013	-0.001	1.1292	0.028	1.1288	0.035

S_{11} e S_{22} are the SWRs.
S_{21} e S_{12} are measured in dB.

1.2 RF cables and connectors

The environment, in which the WPMs work, taking care of RF and cryogenic compatibility, has dictated the choice of the technology for the 144 coaxial cables. In particular the dielectric must be radiation resistant and the conductor size and material has to be chosen to limit the cryogenic losses at 2 K, while guaranteeing adequate RF performances.

The solution has been found together with Suhner, developing a new cryogenic, radiation resistant, coaxial cable (P02182-02 NT). The inner coaxial is a copper clad steel (ASTM B452) wire, the outer conductor is a silver plated, copper clad steel braid and the dielectric is Peek (polyetheretherketon). All the SMA connectors and the 50 Ω loads are also employing Peek as dielectric. Figure 9 shows the RF performances of this cable at room temperature. In particular at 140 MHz the total insertion loss given by our 2.4 meters long cable is limited to 1.8 dB, which is an acceptable number for this application.

With a proper heat sinking at the 4.5 K and 70 K levels, the computed heat load at 2 K produced by each cable is 18 mW, which gives a total heat load of 2.5 W for the 144 cables installed in cryomodule prototype. The global static losses of the module at 2 K, measured once installed and in operation[1], are consistent with this estimation. In fact the measured static losses at 2 K added up to 6 W, to be compared with the 2.8 W estimated, that do not include

the two optical windows (0.5 W each) used in the prototype for independent alignment checking.
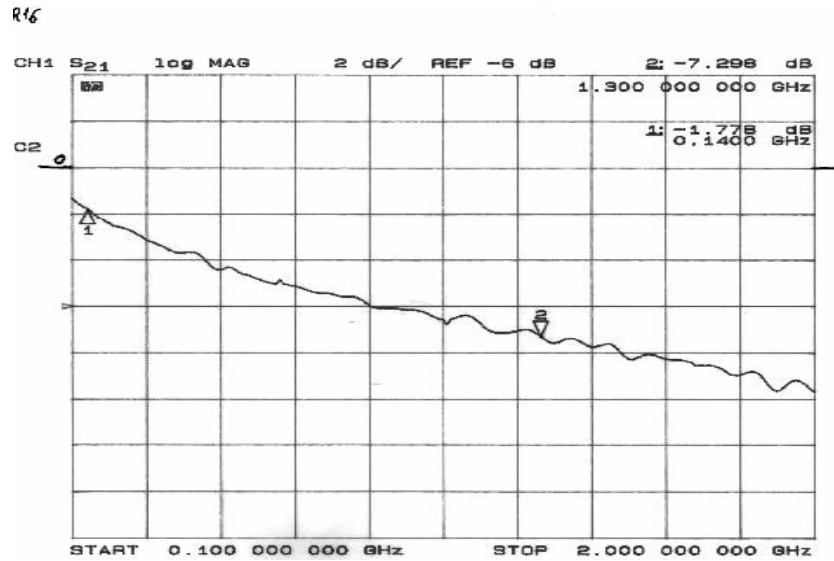
FIG. 9: Insertion Loss for a typical P02182-02 NT cryogenic RF cable.
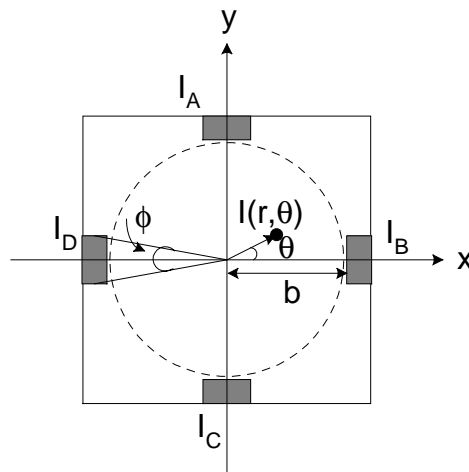
FIG. 10: Bi-dimensional model of the WPM.

2   PRINCIPLES OF OPERATION

The principle of operation of the WPM is well described in the literature about the directional coupler BPMs[3]. The quantity of interest is the difference signal between two opposite micro strips, which is function of the wire (or beam) displacement from the monitor axes. The measure is then normalized to the sum of the two opposite electrode signals, to be independent from the magnitude of the RF signal traveling on the wire. To investigate the WPM behavior we can use a simple bi-dimensional model, as shown in figure 10. If the wire displacement is not too far from the center (i.e. if the wire is not too close to the WPM walls),

we can consider the microstrip as a part of a circular conductor, surrounding a current placed in its center of magnitude

$$I' = I\frac{r}{b} \tag{3}$$

where r is the wire displacement from the center and b the distance between the microstrip and the center (i.e. the circle radius).

According to Shafer the current induced on the microstrip B is

$$I_B(t) = -I(t)\frac{\phi}{2\pi}\left\{1 + \frac{4}{\phi}\sum_{n=1}^{\infty}\frac{1}{n}\left(\frac{r}{b}\right)^n \cos(n\vartheta)\sin\left(\frac{n\phi}{2}\right)\right\} \tag{4}$$

and the induced current on the opposite microstrip D is

$$I_D(t) = -I(t)\frac{\phi}{2\pi}\left\{1 + \frac{4}{\phi}\sum_{n=1}^{\infty}\frac{1}{n}\left(\frac{r}{b}\right)^n \cos(n\vartheta)\sin\left[n\left(\pi + \frac{\phi}{2}\right)\right]\right\} \tag{5}$$

What we measure on each upstream port is the voltage $V = I\cdot Z_0$. The quantity of interest is the normalized difference signal, i.e.:

$$D_x = \frac{V_B - V_D}{V_B + V_D} = \frac{4\sin(\phi/2)}{\phi/2}\cdot\frac{x}{2b} + \frac{2\sin(3\phi/2)}{3\phi/2}\cdot\left[\left(\frac{x}{b}\right)^3 + \frac{3xy^2}{b^3}\right] \tag{6}$$

neglecting higher order terms.

In the same way we can compute the vertical position y.

$$D_y = \frac{V_A - V_C}{V_A + V_C} = \frac{4\sin(\phi/2)}{\phi/2}\cdot\frac{y}{2b} + \frac{2\sin(3\phi/2)}{3\phi/2}\cdot\left[\left(\frac{y}{b}\right)^3 + \frac{3x^2y}{b^3}\right] \tag{7}$$

The larger is the wire displacement from the WPM center the more significant are the non-linear terms.

The expressions (5), (6) and (7) are not very handful to be solved to compute the wire position. A more practical method is to put the wire in well-known position, to measure the related microstrip signals and to find the functions x = f(Dx, Dy) and y = f(Dx, Dy) using a 3D fitting program.

A test bench has been constructed for mapping the response of single WPMs. The wire is mounted in a fixed position and the 140 MHz RF signal is applied to it from the RF&LO generator box. The WPM is assembled on a two axis translation stage and can be positioned

anywhere within its aperture. Our map has been done on a squared section of 6 mm side across the center of the WPM (± 3 mm around the center), with steps of 0.2 mm, in order to fit the data in the actual WPM working region. The translation stage is composed of two slides driven by stepping motors. All the facility is mounted onto an optical table, to minimize position errors. The absolute accuracy of the positioning system is repeatable within 10 μm.

The structure is 1.2 meters long with the WPM mounted between two sections of pipe, which presents the real boundary conditions of the working environment. Two RF transformers before and after the 180 Ω line are used to minimize the SWR. A four channels electronic board (which will be described in great details in a successive paragraph) is used to read the microstrip signals. A PC running LabView program controls the entire process of WPM mapping. In figure 11 the block diagram of the WPM mapping system is shown.
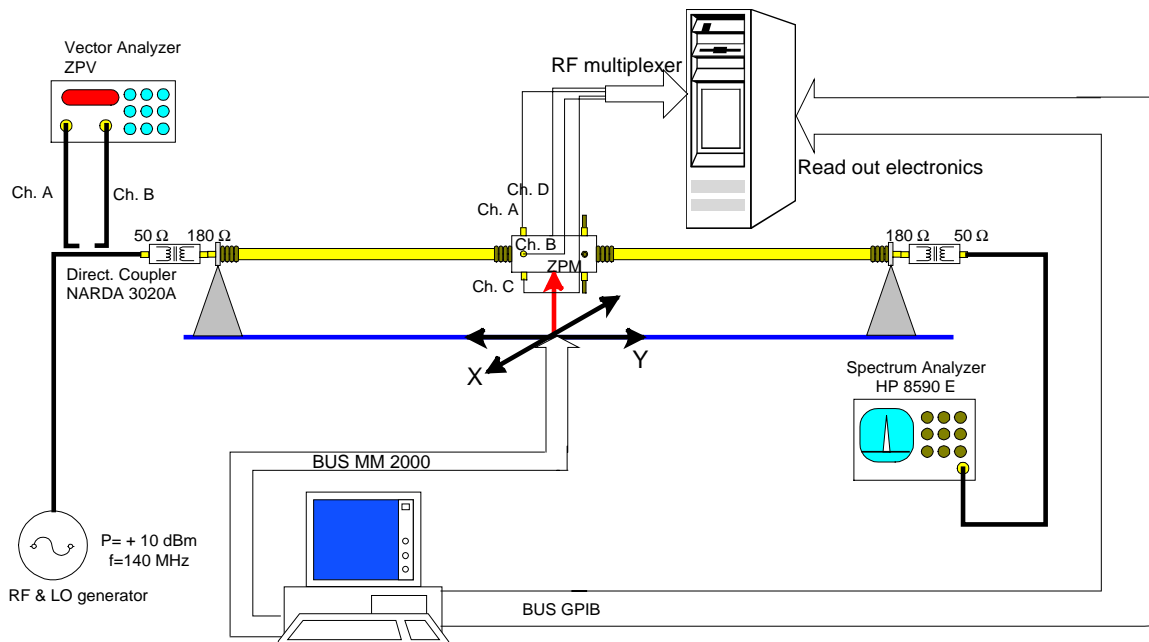
FIG. 11: Block diagram of the WPM mapping system.
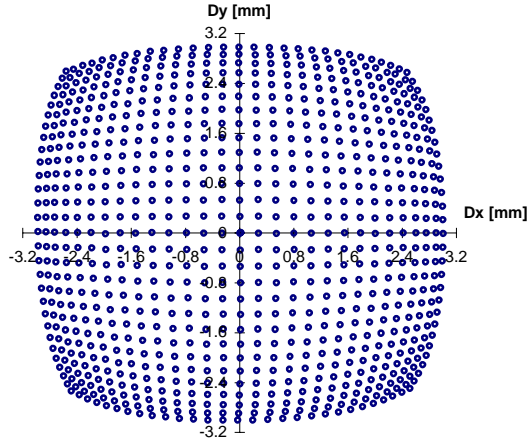
FIG. 12a: Typical WPM's D_x,D_y points map.

A typical WPM map is shown in figure 12a. The graph has D_y and D_x on the vertical and horizontal axis respectively, properly scaled to be comparable with the imposed wire position. The non-linearity arising when the wire is displaced more than 1 mm from the center is evident. Two data sets are produced, one for each axes. In picture 12b the data map for the y-axes vs. Dx and Dy is shown. The data are fitted using TableCurve 3D.
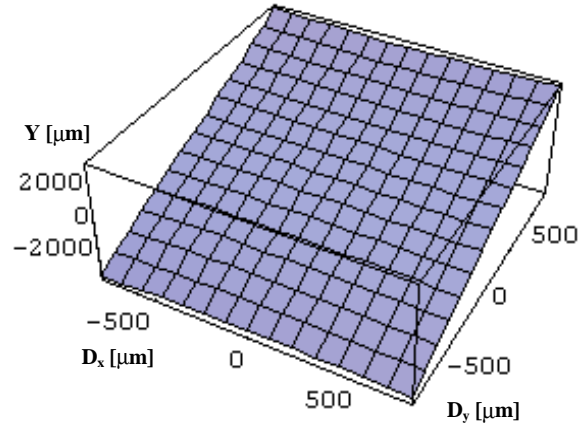
FIG. 12b: Plot of y as a function of D_x and D_y

Fitting the data with a 3rd order polynomial, we get:

$$x = a_{10}D_x + a_{30}D_x^3 + a_{12}D_xD_y^2$$
$$y = a_{01}D_y + a_{03}D_y^3 + a_{21}D_x^2D_y$$

(8)

Actually each polynomial has ten coefficients a_{ij}, but only the ones shown in the equations (8) are significant, the others being due to set up errors or mechanical imperfections and of lesser weight. All this is in agreement with equations (6) and (7).
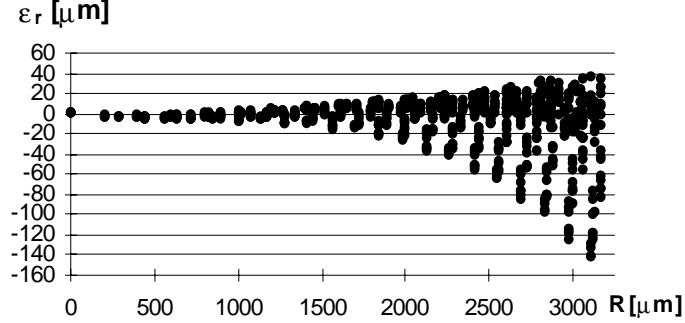
FIG. 13: Error in the wire position measurement, as a function of its distance from the WPM's center, computed using the simplified fitting of equation. (8).

The error in position measurement, using the simplified fitting discussed above, is shown in figure 13 as a function of the wire displacement from the monitor center. We note that at 3 mm from the center the error diverges to more than 0.1 mm. If higher accuracy is required for larger displacements (with respect to the monitor internal diameter), higher order terms of the fitting polynomial have to be added, but this is useful just if the monitor tolerances and the absolute position accuracy are improved too.

3   CONTROL ELECTRONICS

The electronics, which handles the signals coming from the WPMs, has been designed according to the Bpm electronics used at Sincrotrone Trieste[4]. A characteristic of the whole design is that the electronics is completely controlled by an external CPU, which provides gain control, synchronization signals and data handling capabilities. Such a feature reflects in a simpler analog electronics and provide and easier way to calibrate and control the board.

The detector electronics has been developed according to the VXI format, in order to improve noise immunity and to take advantage of the larger board size. Each board will accommodate the components for the control of two WPMs. The interface toward the CPU (which is an Eltec Eurocomm 17, 68040 based @33 MHz with FPU) is based on VME.

Each module is composed of three parts: the RF input, the IF/AGC/Integrator and the ADC/DAC/timing part. The block diagram is shown in figure 14. The input stage is a four channel RF multiplexer used to switch the signals coming from each WPM to a common read out and processing circuitry. The multiplexer is based on HP 5082 pin diodes that ensure very high linearity. The RF 140 MHz signals, after being amplified of 20 dB through a MAR 6 RF amplifier, are down-converted to the 10 MHz IF frequency signal with a double balanced mixer. Both the RF and the LO 150 MHz signals are generated with a PLL synthesizer placed in an external module. The IF signal is applied to a Automatic Gain Amplifier (AGC) module,

that keeps the detector stages at the same output level, 90% of the Analog to Digital (AD) converter, whatever is the detected signal.
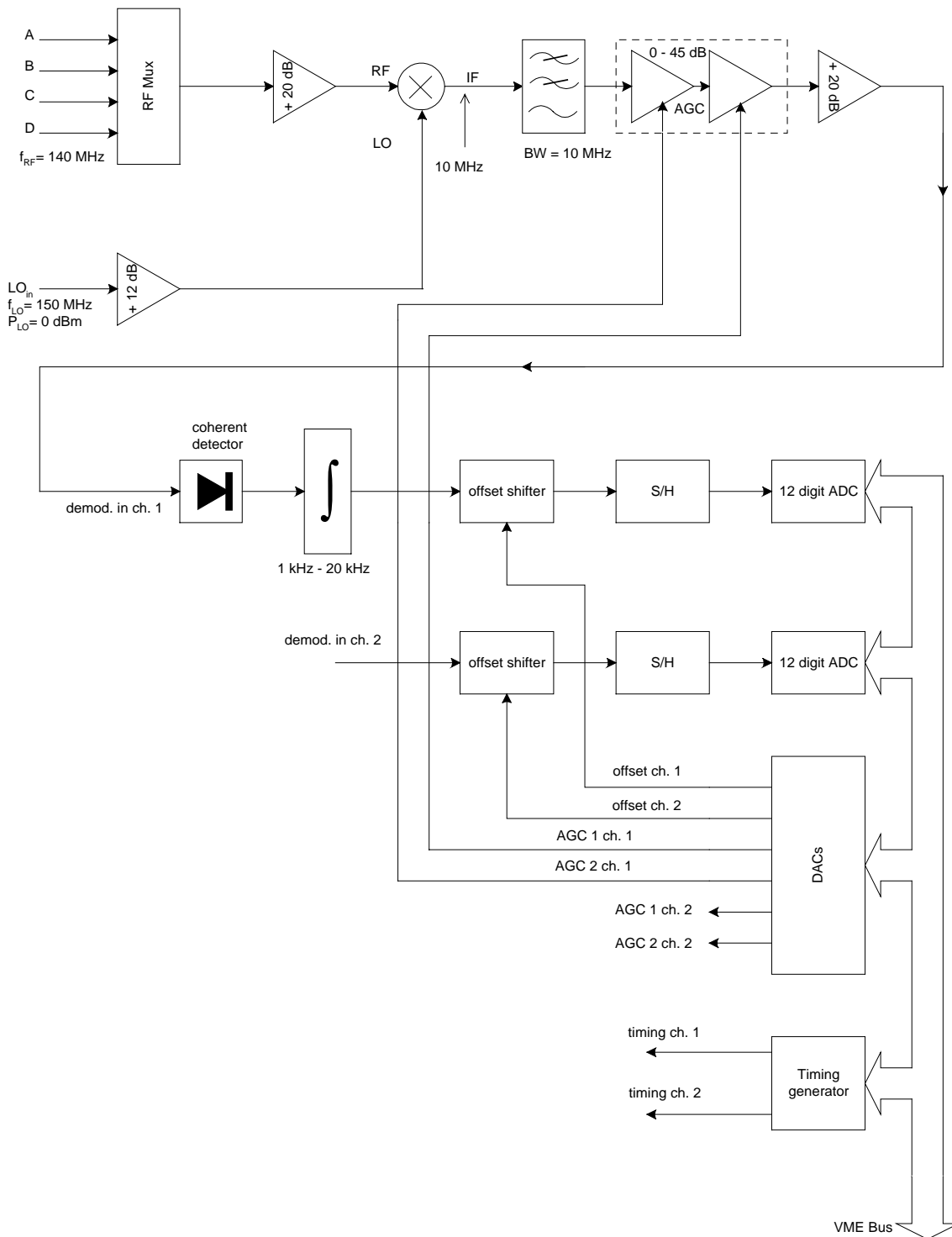
FIG. 14: Block diagram of the wpm control electronics

In this way the AD converter can always work close to its maximum value where that corresponds to its best resolution, and even strongly excentered positions of the wire can be

detected without the risk of saturating the converter. The AGC circuit is based on two BF966 Mosfet amplifiers. The gain is varied applying a control voltage on the Mosfet gates. The control voltages are provided by an 8-bit Digital to Analog Converter (DAC) for the first stage, and by a 12 bit DAC for the second one, that performs the fine adjustment in the AGC gain.

The amplitude detector is a synchronous detector based on a XR 2208 analog multiplier. It has 40 dB of dynamic range with a ± 0.1% linearity. The integrator cut off frequency is set by the software to be 1 kHz or 20 kHz according to the selected operating mode. The latter is the maximum rate of acquisition, keeping in mind that the minimum process time for a single microstrip is 50 μs. Under operating conditions the acquisition rate is 1 kHz.

The ADC/DAC/timing part requires several software controls, like real time reading of the ADC values. The other required functions are the selection of the timing rate, the setting of the DACs for hardware-compensated amplitude detector 'zero offset' value and the setting of the DACs for the Automatic Gain Controls. A on board timing generator circuitry is provided, even if normally is not used, being preferred for this purpose an external clock and synchronisation circuit, common to all the detector boards.

The RF input part is critical for the accuracy of the wire position calculation, therefore the input stage and the annexed cables from the microstrips connectors must be calibrated on field to compensate the little differences among the four channels and to minimise eventual impedance mismatches. At the same time, for each amplitude detector the best zero offset value must be found with a proper calibration routine. These calibration values are then stored in a configuration file.

On line control of the detector electronics and handling of data acquisition from each one of the two structures is performed by a VME 68040 CPU fitted inside each VXI crate. Raw data acquisition, averaging and corrections with polynomial curve are performed at this level. A local storage of data has been provided before a transfer will occur toward a dedicated NFS server. This machine allows sharing data between consumer processes. A PC with a LabView based application provides console functionality for the whole system. On line monitoring of each set of WPM along with analysis of the displacement of each WPM versus time may be done using a menu driven interface. Advanced data processing (frequency analysis, power spectrum of any instability, etc.) is available as a powerful tool to analyse the possible vibrations of the structure.

3.1   RF & LO generators

The RF, f = 140 MHz, signal is generated by a VDS 1550B PLL frequency synthesizer (from SCITEQ Electronics, Inc). The VDS 1550B output signal, +10 dBm of amplitude, is applied via the MCL ZFSC-2-1 Power Splitter to the RF Section of the rack. The block diagram of the RF & LO is shown in figure 15.

The RF section is composed of the following devices (from input to output):
- MCL ZDC-10-1 10 dB coupling directional coupler. The coupled port is accessible through a BNC female connector on the front panel to test the RF signal (RF pick up);

- JFW 50TA-007 coaxial stepping attenuator. This device is used to control the RF signal amplitude in 0.5 dB steps (RF output control push buttons on front panel). This value, set experimentally on field, has to take into account the signals attenuation due to the very long coaxial cables used to interconnect the WPM and the electronics cabinet in the Hall 3 at DESY.
- MCL PSW 1211 RF Switch;
- MCL ZFSC-2-1 power splitter;
- two MCL ZHL 3A power amplifier (1 W max output power). These two power amplifiers deliver the RF signal to the RF input connectors placed on the two WPM lines end caps.

The 150 MHz LO signal is generated mixing the 140 MHz RF signal with a sample (+7 dBm) of the 10 MHz reference signal. A coaxial DC block uncouples the auxiliary VDS-1550B reference signal output from the local oscillator port of the mixer.
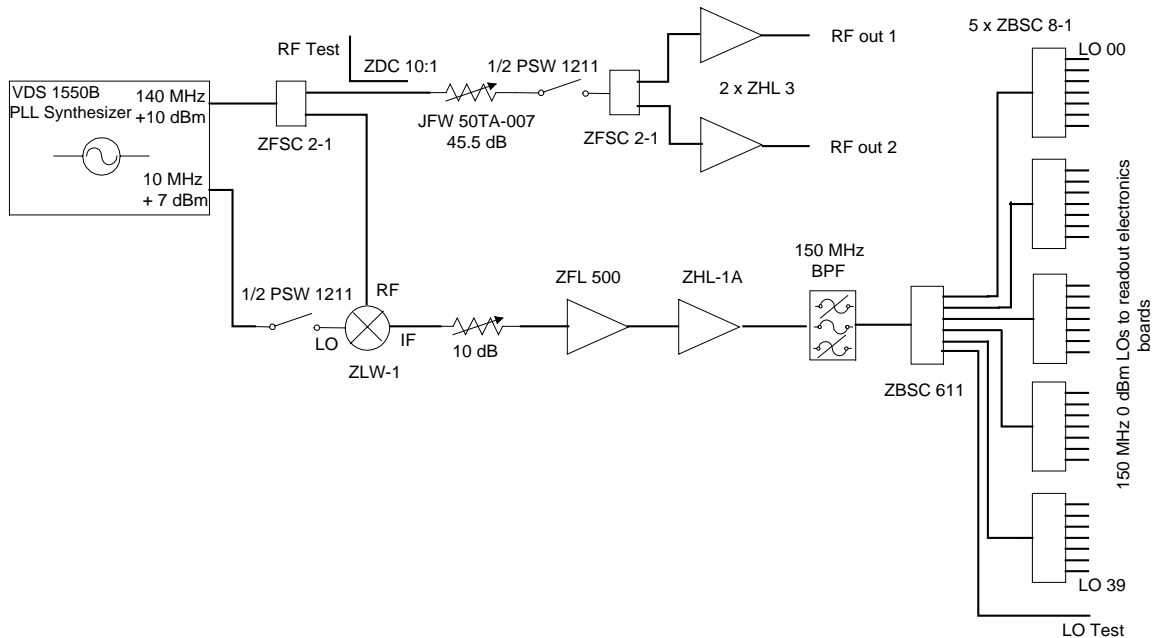
FIG. 15: RF & LO generator block diagram.

The LO section is composed of:
- MCL ZLW-1 frequency mixer;
- MCL ZFL 500 low noise RF amplifier;
- MCL ZHL-1A power amplifier (500 mW);
- K&L 150 MHz band pass filter, used to reject all the spur intermodulation products;
- MCL ZBSC-611 six way power splitter;
- Five MCL ZCSC-8-1 eight way power splitters. These "tree" of splitters provides the 40 LO outputs placed on the rear panel (female SMA connectors). Actually the control

electronics cabinet contains 18 readout boards, each one needing two 0 dBm ($\pm$ 1 dB) LO signals. The residual sixth port of the ZBSC-611 is connected to a female BNC connector on the front panel to provide a LO test signal.

The RF&LO rack is connected via a 6 pin VEAM connector to a power supply rack, that is left always on to ensure high stability to the reference oscillator frequency.

Two toggle switches placed on the front panel controls the PSW 1211 coaxial switches on the RF and LO lines. When the RF switches are open the high frequency signals are terminated on internal 50 Ω loads.

The RF & LO rack specifications can be found in Appendix I.

4 COOLDOWN AND WARMUP OPERATION RESULTS

Three complete thermal cycles have been done on the first cryomodule. In the figures 16 and 17 the historical sequence of the first two complete thermal cycles, as measured by selected WPMs, is shown. For readability reasons not all the WPMs result are shown in the pictures, but only the most representative ones. Actually, WPM1 and WPM18 are the first and the last of the monitors' chain, while the three cold mass posts lie in correspondence of WPM3, WPM9 (the central post) and in between WPM15 and WPM16.
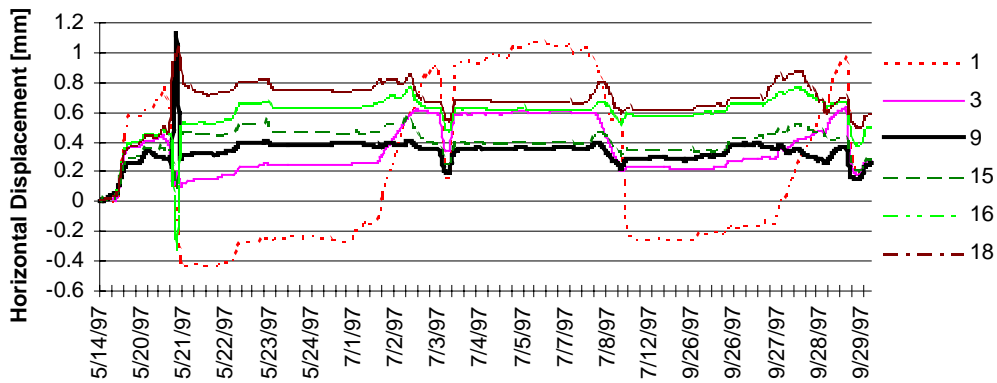
FIG. 16: Historical graph of the horizontal displacement of the first TTF cryomodule cold mass during the first two cooldown and warm up operations.
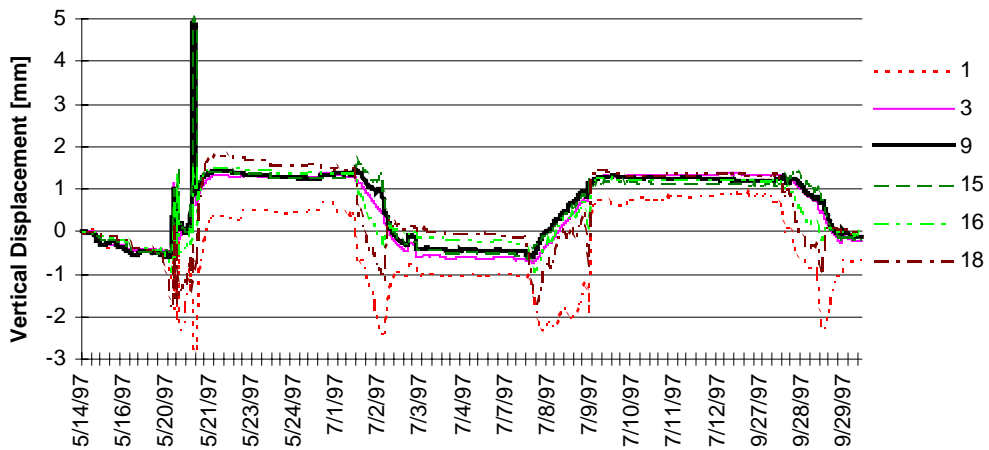
FIG. 17: Historical graph of the vertical displacement of the first TTF cryomodule cold mass during the first two cooldown and warm up operations.

The data are normalized to the positions read on the 13th of May 1997, at 17:00, just after the cryomodule was completely closed. The graphs show the displacements of the center

of the Linac (the beam tube), computed with the signals sampled by the sensors, that are fixed along two symmetrical (with respect of the beam tube) straight sections.

During the cooldown, the cold mass is expected to perform a vertical drift of about 1.5 mm, and a symmetric contraction of about 0.5 mm on the horizontal plane[1].

The cryomodule pump down started on May 14, and lasted for about one week. At the beginning of figures 16 and 17 one can see a movement of the cold mass of about 0.5 mm towards the positive direction, both vertical and horizontal, as an effect of the vacuum pumps.
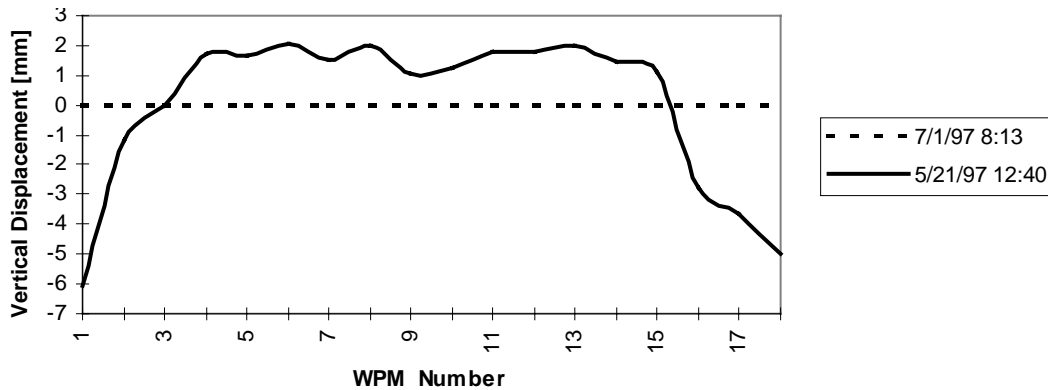
FIG. 18: Taking as a vertical reference the stable cold position after the first cooldown (7/1/97), the solid line (5/21/97) shows the maximum vertical bending of the cavity string during the fast cool down.

The cooldown procedure started on May 20. As planned, the cavities were cooled through the cool down - warm up tube, in parallel with the 4 K shield, the fluid temperature being controlled to limit the maximum temperature difference inside the structure to 50 K, as suggested by the FEM calculations. A decreasing fluid temperature is obtained by mixing warm He gas to the cold box 4 K output. Cooling of the so-called 70 K shield is performed via a second cold box output. An abnormal vertical shift is shown on the vertical displacement graph. This graph shows the effect, as detected by the WPMs, of a fast cooldown performed on the cavity string, to check the possibility of preventing hydrogen driven Q disease in unbaked cavity, by a fast crossing of the 100 K region. This procedure has produced a large bending due to the thermal conductivity of the cavity supports versus the lower part of the He gas return pipe (He GRP), whose cool down was much slower. FEM simulations demonstrated that an average difference of 8 K between the lower and the upper temperature of the He GRP is enough to produce this effect. This experience showed that a pre-cooling to 100 K (instead of 130 K) of the He GRP would have prevented this effect that, in any case, has been completely recovered once the final temperature is reached. Actually, this abnormal vertical shift is not completely due to the cold mass movement, but an undesired wire drift due to the external coaxial tubes is added. This undesired drift that partially distorts the cryostat bending detection, is a result of the reduced monitors clearance caused by the

problems in aligning the WPM strings we talked of in the first paragraph. The effective WPM aperture was heavily reduced to about 3 mm in spite of the 12 mm designed.

A behavior closer to the reality of the cold mass during the fast cooldown is shown in figure 18, after the wire (estimated) drift has been subtracted.
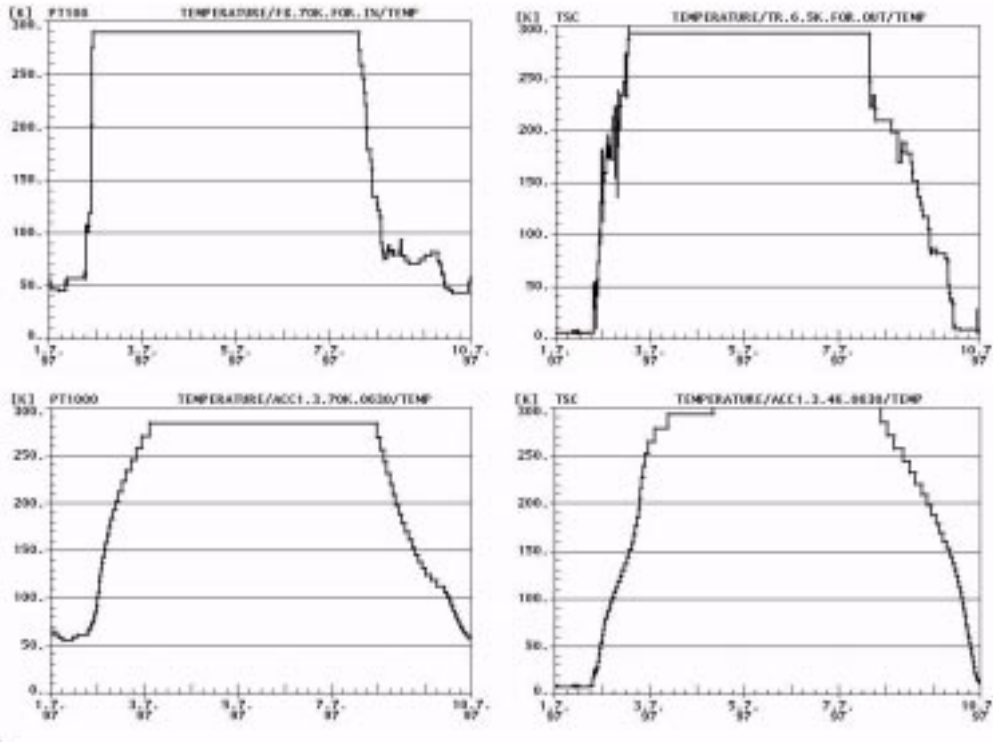
FIG. 19: Temperature curves during the warmup and cooldown performed at the beginning of July.

A better procedure was followed during the successive warmup and cooldown procedures, where the bending has been contained.

The warmup operations started on July 1 and ended on July 3. The second cooldown operations started the 7th of July and lasted until the 10th of July. The temperature graphs in figure 19, are relative to the warmup and cooldown operations performed in July, and associated to the historical graphs lead to a complete understanding of the cold mass behavior. The two upper curves show, as a function of time, the input temperatures of the cooling Helium, after the mixing with the warm gas and before the entrance in the cryomodule, respectively for the 70 K (left) and the 4K (right) circuits. The two lower curves, to be compared with their upper curves, show the behavior of the worst temperature in the two shields respectively.

The second warmup started on September 27 and ended on September 29. In the same day the pressure was raised again to 1000 mb, as one can see from the horizontal position abrupt shift. From the historical graphs one can see the expected 1.5 mm (nominal) vertical drift, where the horizontal displacement graph shows a center drift due to the presence of

asymmetric forces acting on the He gas return pipe. Conversely the reproducibility between two successive cooldown (and warmup) has been demonstrated to be very good.

The figures 20 - 23 show the cold mass stable positions during thermal operations as measured by the WPMs, during stable (from the thermal point of view) positions. In particular, the graphs shown in figs. 20 and 21 display the cold mass behavior during the first cooldown and warmup operations, while figures 22 and 23 are related to the second complete thermal cycle. All the curves are normalized to the stable warm position "13/5/97 17:00".
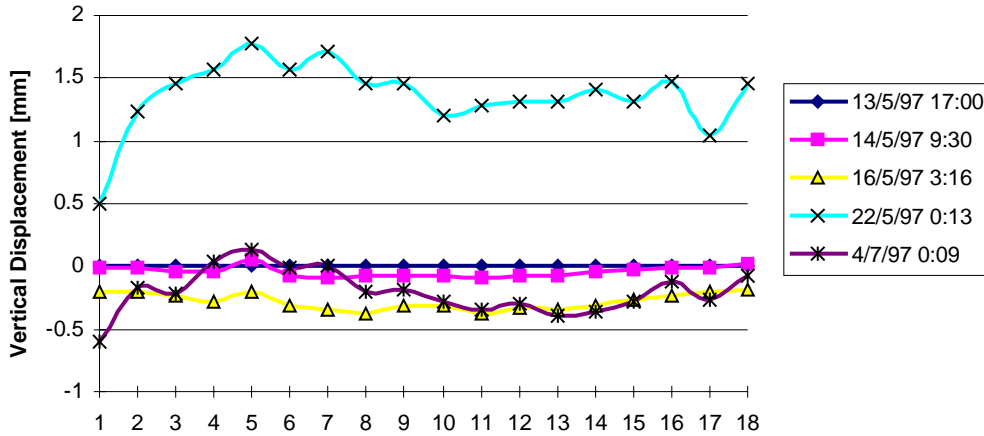
FIG. 20: Vertical displacements related to stable positions during the first complete thermal cycle.
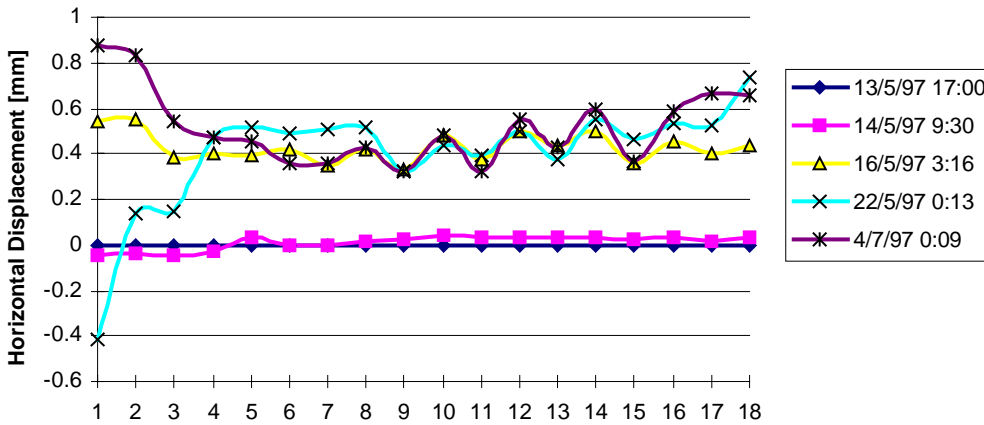
FIG. 21: Horizontal displacements related to stable positions during the first complete thermal cycle.

From figures 20 and 21 we see that the vacuum pumping (curve "16/5/97 3:16") produces a negative vertical movement of the cold mass of about 0.3 mm, and a right shift of the beam line center of about 0.5 mm. After the cooldown is completed, (curve "22/5/97

0:13"), the cold mass has performed the expected positive vertical displacement induced by thermal shrinkage, of about 1.5 mm. The horizontal misalignment is also evident.

The stable warm position is well recovered for the vertical displacement after the warm up, as seen from the curve "4/7/97 0:09".
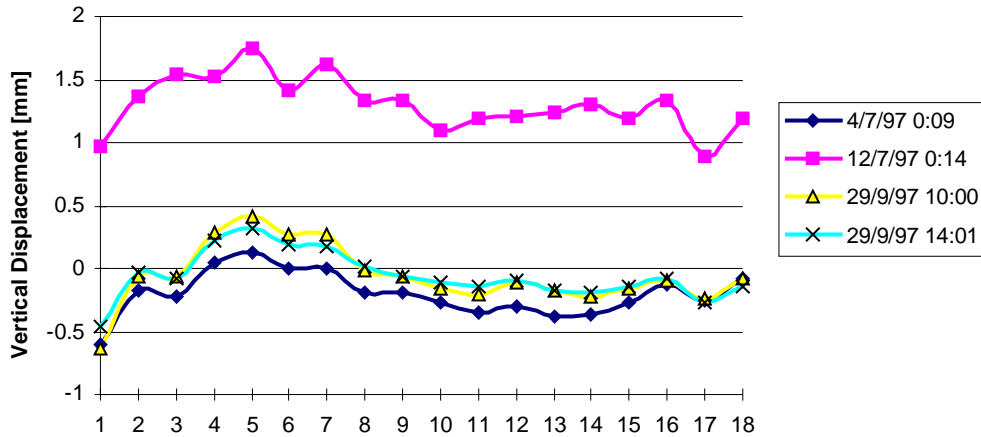
FIG. 22: Vertical displacements related to stable positions during the second complete thermal cycle.
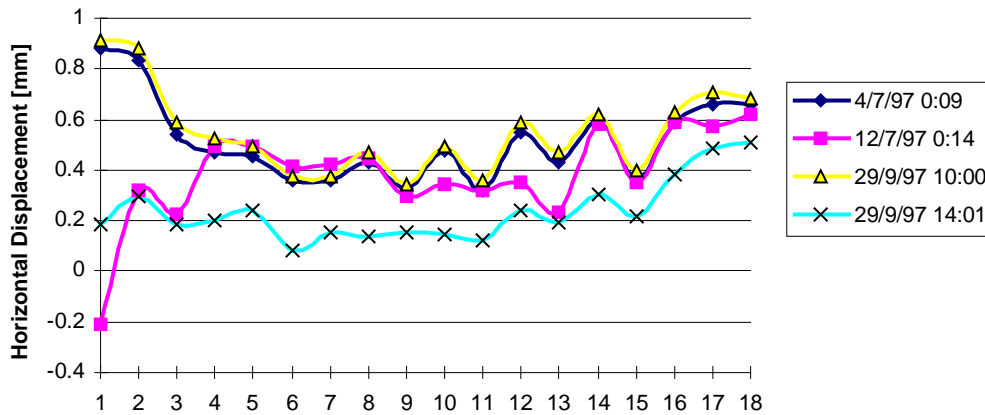
FIG. 23: Horizontal displacements related to stable positions during the second complete thermal cycle.

During the second thermal cycle, we can appreciate the good reproducibility between two successive cooldowns and warmups. For a well understanding of the graphs, we summarize as a legenda, the stable positions, referring to the dates the physical situation of the cryostat.

N.B.: The positions are all referred to the stable warm position 13/5/97, 17:00.

- 14/5/97 h 9:30   Starting of the vacuum pumping.
- 16/5/97 3:16   Pressure = 0.1 mb; T = 300K.
- 22/5/97 0:13   Stable cold position after first cooldown operation.
- 4/7/97 0:09   Stable position after warm up; pressure = 0.1 mb.
- 12/7/97 0:14   Stable position after second cooldown.
- 29/9/97 10:00   Stable position after second warm up; pressure = 0.1mb.
- 29/9/97 14:01   Stable position after second warm up; pressure = 1000 mb.
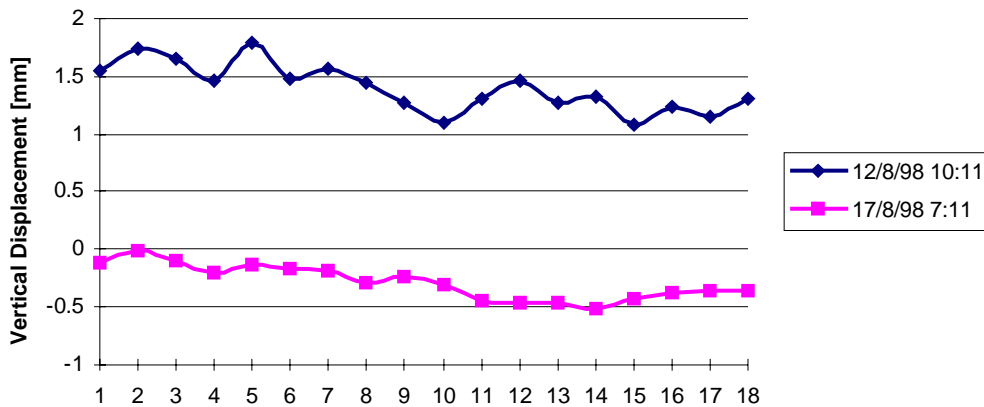
FIG. 24: Vertical displacements related to stable positions 23/11/98 during the third complete thermal cycle.
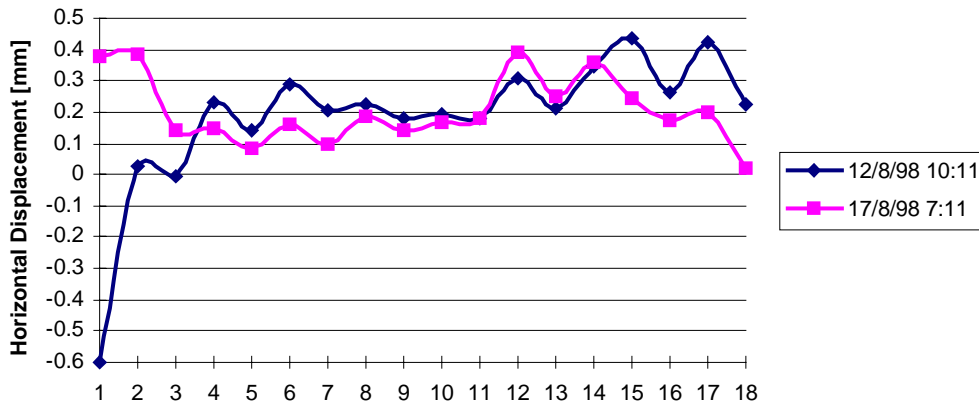
FIG. 25: Horizontal displacements related to stable positions 23/11/98 during the third complete thermal cycle.

The two figures 24 and 25 show the third cooldown and warmup operations. The third cooldown started at the end of January 1998 after a cryomodule opening. The positions are referred to the stable warm position of 23/1/1998 at 15:25, just before the start of the

cooldown. The cryomodule was left cooled till the mid of August. The warm up started on the 13th of August.

The cryostat was opened to let some technical operations on damaged parts, between the second warmup and the third cooldown. In spite of this, during the third thermal cycle we still have well reproduced the behavior of the two former thermal cycles.

5   IMPROVED WPMs FOR THE 2ND AND 3RD TTF CRYOSTATS

The experience gained so far led us to some changes in WPM design. An all-internal simplified new generation WPM system has been designed to be installed in the second and third cryomodules string[5].

For each cryomodule only one chain of 9 WPM is inserted. Each monitor is placed at the beginning of each active cryo-unit.
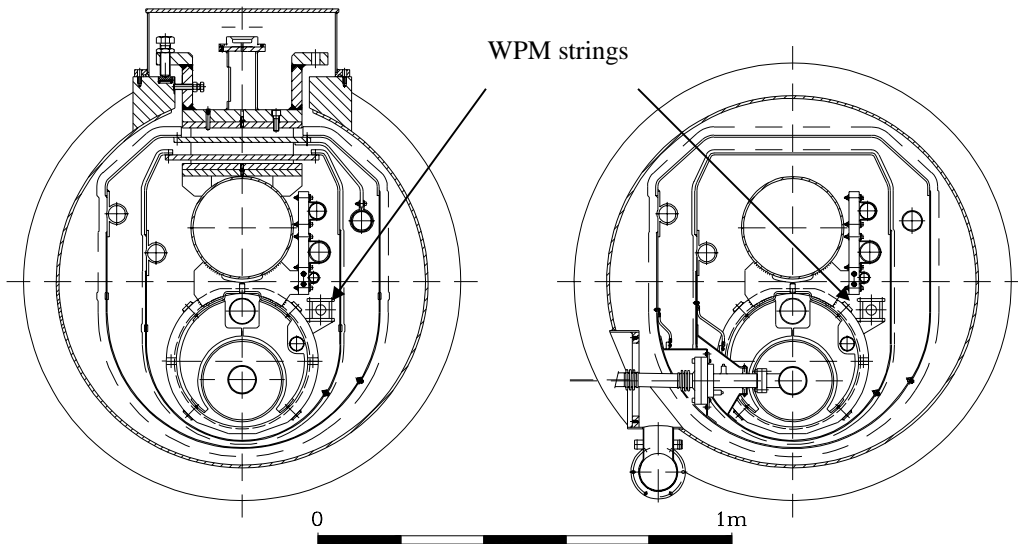
FIG. 26: Second generation cryomodule cross section, showing WPM string positions.

In figure 26 the cross sections of the cryomodules string 2 and 3 show where the WPM chains are placed.

Each WPM is directly screwed to its supporting brackets instead of the complicate supporting frames, with moveable positioning screws, of the first device. The WPM fixed to its supporting arm is shown in figure 27.

The monitor geometry has been changed too. The WPM clearance is now of circular shape, in spite of the squared shape of the former version. The diameter of the circular section is of 28 mm instead of the 12 mm of the previous WPM aperture. Moreover the monitor is composed of only one aluminum block, in opposition to the first cryostat WPMs, that were composed of two parts, to be screwed together.
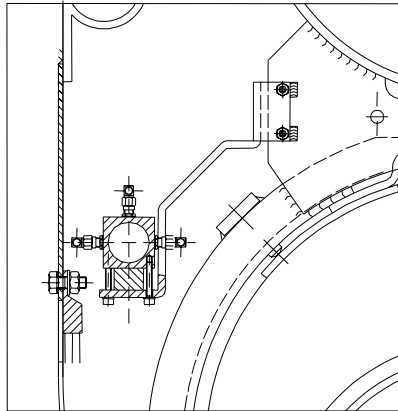
FIG. 27: New generation WPM screwed to its supporting arm.
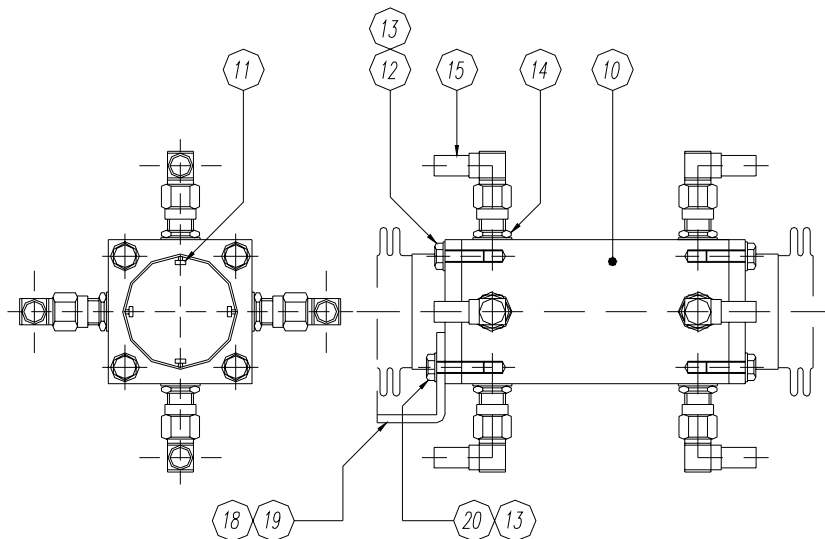
FIG. 28: New generation WPM cross and lateral views.

The new monitor is shown in figure 28. One of the major advantages of these modifications on WPM geometry is an increased clearance; in order to avoid unwanted wire drifts during the cooldown operations. Moreover the monitors chain assembling and aligning operations will be easier. Last but not least, the detector linearity region is now more than doubled, spanning on a region of ± 3 mm across the center. This, in our expectations, will lead to a reduction in the position reading errors.

The new generation WPM main features, together with the results of thermal operations on the second TTF cryostat, will be object of a further note.

6 APPENDIX I - RF & LO Generator Specifications

Here follow the RF & LO rack specifications.

6.1 RF Section

Frequency	140 MHz
Output Power	-18 ÷ + 27 dBm in .5 dB steps
Output Power Control	7 bits, manual (push-buttons on front panel)
Harmonics	< -20 dBc
Spurs	< -60 dBc
Phase Noise	< -85 dBc/Hz @1kHz offset
	< -95 dBc/Hz@10 kHz offset
	< -110 dBc/Hz@100 kHz offset
Output Impedance	50 Ω nominal

6.2 LO Section

Frequency	150 MHz
Output Power	+1 dBm
Harmonics	< -50 dBc
Spurs	< -60 dBc
Phase Noise	< -83 dBc/Hz@1 kHz offset
	< -95 dBc/Hz@10 kHz offset
	< -105 dBc/Hz@100 kHz offset
Output Impedance	50 Ω nominal

6.3 Frequency Reference

Source	10 MHz, Internal
Stability	± 1 ppm/year
Burn in	48 hours

6.4 Connectors

RF Out	N female (2) on rear panel
LO	SMA female (40) on rear panel
RF Pick Up	BNC female on front panel
LO Test	BNC female on front panel

6.5 Power Supply

+24V @ 2.5A
+5V @ 8A
+15V @ 2A
-15V @ 0.7A

6.6 Environmental

Operating Temperature	0°C to +50°C
Storage Temperature	-20°C to + 70°C

7 ACKNOWLEDGEMENTS

8 REFERENCES

(1) C. Pagani et al., Construction, Commissioning And Cryogenic Performance Of The First Tesla Test Facility (TTF) Cryomodule, in Proc. of the 1997 CEC/IMC, (Portland, 1998)

(2) T. Edwards, Foundations For Microstrip Circuit Design, 2nd edition (Wiley & Sons, 1992).

(3) R. E. Shafer, Characteristics Of Directional Coupler Beam Position Monitors, IEEE Trans. Nucl. Sci. 32, 1933 (1985).

(4) R. De Monte et. al., Elettra BPM System (Hardware and Software): First Results, in Proc. EPAC 1994, 1530, (1995).

(5) D. Barni et al., Towards the Third Generation of TTF Cryomodule, Tesla note n. 98-16 (June 1998).